

Intrinsic structure of relaxor ferroelectrics from first principles

Xinyu Xu^{1,2,*} Kehan Cai^{3,*} and Pinchen Xie^{1,†}

¹*Applied Mathematics and Computational Research Division,
Lawrence Berkeley National Laboratory, Berkeley, CA 94720, USA*

²*Department of Materials Science and Engineering, Stanford University, Stanford, CA 94305, USA*

³*Department of Chemistry, Princeton University, Princeton, NJ 08544, USA*

(Dated: November 21, 2025)

We hybridize the swap Monte Carlo and geometric relaxation methods to determine the intrinsic compositional structure (CS) of the lead magnesium niobate (PMN) relaxor. We verify the stability of a Nb-rich sublattice in PMN, as prescribed by the prevailing random-site model. However, ions in the complementary sublattice are not randomly mixed. Most Nb ions collapse into a single percolating cluster with a mesh-like structure. This specific geometry serves to prevent large space charges, and this behavior differs from typical phase separation in metallic alloys. Subsequent molecular dynamics simulations predict a pair distribution function that is consistent with neutron scattering experiments. Analysis of dipolar structures in the Nb cluster sheds light on the unique dielectric properties of PMN.

Relaxor ferroelectrics are glass-like crystals susceptible to electric fields over a wide range of temperatures and frequencies [1–8]. What makes relaxors unique is the compositional disorder that disrupts the homogeneous structural distortion associated with bulk ferroelectricity in conventional ferroelectrics [9].

A major family of relaxors consists of complex perovskites with the general formula $AB_xB'_{1-x}O_3$. A prototypical relaxor in this family is the $Pb(Mg_{1/3}Nb_{2/3})O_3$ crystal, also known as PMN, where the arrangement of Mg and Nb ions (B-site ions for brevity) is intrinsically disordered. The consequence of disorder may be understood from the theory of spin glass [10], since compositional disorder implies disordered local fields and coupling frustration. In fact, there is a phenomenological resemblance between the frequency-dependent peak in the permittivity of relaxors and a similar behavior found in spin glasses [10, 11]. However, the similarity does not validate the assumption of homogeneous disorder, as typically adopted in spin glass models. The intrinsic compositional structure (CS) of many relaxors is yet to be clarified. PMN is of particular interest because Mg and Nb differ in valence, in contrast to equal-valence relaxors such as $BaZr_xTi_{1-x}O_3$. The anatomy of PMN’s CS may hold the key to understanding the CS of generic non-equal-valence perovskite solid solutions, which can be essentially different from those of disordered alloys.

Various models for PMN CS were under debate [5, 12–21]. There were two prevailing ones. The first is the charge-balanced random-site model [16] (also known as the random-layer model) that involves the two interpenetrating face-centered cubic sublattices (denoted β^I and β^{II}) of a perovskite structure. The random-site model prescribes that B sites on β^{II} are occupied almost exclusively by Nb ions [22], while β^I contains a random mixture of Nb ions and Mg ions in a 1:2 ratio. The second is the space charge model [12], where $PbNb_{1/2}Mg_{1/2}O_3$ clusters subject to rock-salt chemical ordering (rock-salt

clusters for brevity) coexist with $PbNbO_3$ clusters (Nb clusters). Both clusters have net space charges that have to be balanced on the mesoscale. So, it was postulated that the rock-salt clusters are nanodomains with a Nb-ion shell. Over the years, various experiments have approved the existence of the Nb-rich β^{II} structure [12, 21, 23], while there is no concrete evidence to prove the space charge model. Physical intuitions also disfavor the space charge model because of the electrostatic energy concentrated within the charged nanodomains. However, the random-site model is not flawless. Considering the site percolation theory [24] on the three-dimensional (3D) sublattice β^I , we realize that large, spatially charged Nb-rich domains will form on the mesoscale in a random-site model. The hypothesis of the random-site model for β^I needs to be re-examined. We tackle this problem and find a new, unexplored mesoscale CS, which also goes beyond the typical phenomena seen in metallic alloys.

Experimentally, there have been no straightforward imaging results that confirm, reject, or refine existing CS models with certainty. There are major difficulties in solving the 3D CS with conventional methods. For example, annular dark-field scanning transmission electron microscopy can distinguish B-site ions [21, 25]. However, the intensity of the B-site signals is averaged along an axis and smeared, which does not prevent the confirmation of a Nb-rich β^{II} , but it cannot elucidate how Nb and Mg are organized in β^I [21]. A different route is to reconstruct the 3D atomic structure from fitting the X-ray and neutron scattering results on PMN with reverse Monte Carlo methods [26]. Although the average geometric structure extracted this way is reliable, to what degree the CS can also be recovered is uncertain, considering that the correlation between CS and geometric structure is subtle and far from straightforward.

Conventional computational approaches are also restricted. Direct density functional theory (DFT) calculations are limited to relatively small supercells. Ef-

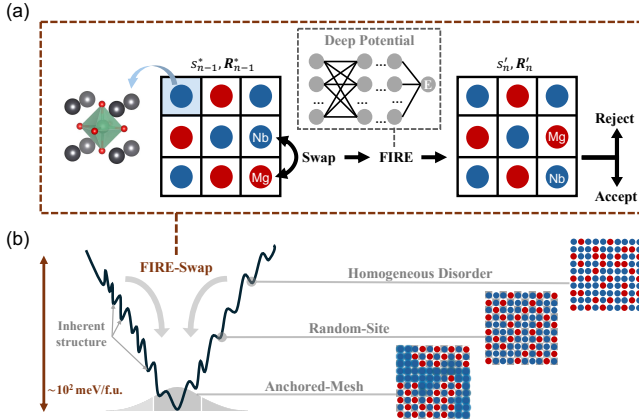


FIG. 1. (a) Sketch of the FIRE-Swap algorithm. (b) Energy stability of different models of CS.

fective atomistic models (effective Hamiltonian [27], all-atom force fields [28], etc) derived from first principles can potentially probe relaxors on larger length scales. However, the existing literature adopts a relaxor supercell with *a priori* CS [29, 30], or optimizes CS with semi-quantitative models with uncontrolled error [31].

The goal of this work is to overcome these barriers and predict the intrinsic structure of PMN with controlled first-principles accuracy. Such a goal is beyond the reach of conventional atomistic models as well as standard Monte Carlo (MC) or molecular dynamics (MD) algorithms. For relaxors, the contribution of atomic geometric disorder to system energy is comparable to that from compositional disorder (see Appendix B). The optimization of compositional and geometric structures cannot be separate. This challenge is universal to disordered materials. Inspired by hybrid methods used to study high-entropy alloys [32, 33], we developed a hybrid structural relaxation method, called FIRE-Swap, based on a potential energy surface (PES) model trained on extensive DFT data covering possible local compositional arrangements and geometric disorder. The PES model for PMN is a Deep Potential (DP) model [34–36] $U(\mathbf{s}, \mathbf{R})$, where $\mathbf{s} = (s_1, \dots, s_N)$ and $\mathbf{R} = (\mathbf{r}_1, \dots, \mathbf{r}_N)$ are the species and positions of all N particles in a periodic simulation box. The model is trained on DFT data with SCAN (strongly constrained and appropriately normed) approximation [37], which outperforms many typical functional approximations for ferroelectrics [38]. The combination of DP and SCAN has also been used to model other ferroelectrics [39, 40]. The construction of the DP model is detailed in Appendix A. In a test set independent of the training data, the root mean square error of the model was ~ 1.0 meV per atom for energy prediction.

FIRE-Swap (see Fig. 1) alternates between (a) geometric optimization with the well-established Fast Inertial Relaxation Engine (FIRE) algorithm and (b) compositional relaxation with MC swapping of the chemical

species of two atoms. For the n -th iteration, step (a) aims to find the inherent structure $\mathbf{R}'_n = \text{argmin}_{\mathbf{R}} U(\mathbf{s}'_n, \mathbf{R})$ associated with a proposed new CS \mathbf{s}'_n that differs from the old CS \mathbf{s}^*_{n-1} . Step (b) calculates the energy cost of swapping: $\Delta E_n = U(\mathbf{s}'_n, \mathbf{R}'_n) - U(\mathbf{s}^*_{n-1}, \mathbf{R}^*_{n-1})$. When $\Delta E_n < 0$, we accept the swapping by letting $\mathbf{R}'_n = \mathbf{R}'_{n-1}$ and $\mathbf{s}'_n = \mathbf{s}'_{n-1}$. When $\Delta E_n > 0$, we accept the swapping with probability $p = e^{-\Delta E_n / k_B T_{\text{FS}}}$, where T_{FS} is the sampling temperature. If rejected, $\mathbf{R}'_n = \mathbf{R}^*_{n-1}$ and $\mathbf{s}'_n = \mathbf{s}^*_{n-1}$. Then a new configuration \mathbf{s}'_{n+1} is proposed by swapping the species of an arbitrary pair of B-site ions that are nearest-neighbor or next-nearest-neighbor in \mathbf{s}'_n . Throughout this paper, the neighboring relation is based on the graph distance of B sites on the simple cubic lattice. So each B site has 6 nearest neighbors and 12 next-nearest neighbors.

In principle, FIRE-Swap samples the equilibrium distribution p_{in} of the discrete set of inherent structures (local minima of PES) [41–43] of a glass-like crystal. It is important to choose a T_{FS} that is small enough compared to the melting temperature T_M such that p_{in} is concentrated on the collection of low-energy inherent structures, i.e., intrinsic structures. A high T_{FS} close to T_M will cause undesirable intensive sampling of more disordered mid-lying CS due to entropic gain. Technically, T_{FS} can not be too small either; otherwise, the simulation will be trapped in mid-lying energy minima because the initial structure is typically a high-energy one. For PMN, we find that $T_{\text{FS}} = 600\text{K}$ balances efficiency and robustness.

Part of the main findings of this work is illustrated by Fig. 1(b), which marks the relative energy stability of CS with homogeneous disorder, the CS prescribed by the random-site model and the intrinsic CS identified by this work as the anchored-mesh model. The CS of the anchored-mesh model are stabler than the CS with homogeneous disorder by roughly 10^2 meV per perovskite formula unit (f.u.) as an order-of-magnitude estimate. The anchored-mesh model still admits a Nb-rich sublattice β^{II} . But the Nb ions on sublattice β^{I} are not subject to trivial random distribution — they form a percolating Nb cluster together with Nb ions anchored on β^{II} . Remarkably, the structure of the percolating cluster does not conform to the phenomenology of standard phase separation. The cluster stabilizes with a dendrite/mesh-like geometry and branches thinly to reduce the space charge, without further coarsening. The 10^2 meV/f.u. energy scale implies that such an intrinsic structure will be difficult to observe on a large length scale in experimental PMN samples, which are typically synthesized at a temperature not substantially below $T_M \approx 1600\text{K}$. Experimental samples [21] will embed a mix of CS in Fig. 1(b), subject to the entropic law.

In the following, we provide evidence for these claims. We first study the stability of the β^{II} filled with Nb ions. We perform a FIRE-Swap simulation of a cubical $6 \times 6 \times 6$ supercell with $T_{\text{FS}} = 600\text{K}$ and the experimental average

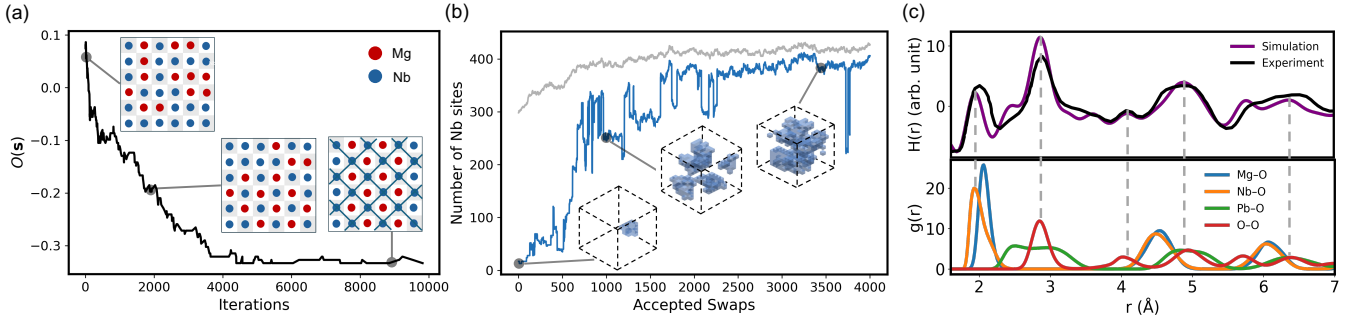


FIG. 2. (a) Order parameter $O(s)$ as a function of accepted FIRE-Swap steps. The insets show the CS of arbitrary cross sections of the $6 \times 6 \times 6$ lattice. sublattice β^{II} are represented by gray tiles. (b) The number of Nb sites in all Nb clusters (gray) and in the largest cluster (blue). The insets show the geometry of the largest cluster in the $12 \times 12 \times 12$ lattice. (c) Upper panel: The predicted (purple) and experimental [26] (black) pair distribution functions associated with neutron scattering of PMN powder samples at $T = 300\text{K}$. Lower panel: The predicted room-temperature radial distribution function.

lattice constant 4.05\AA . The supercell is initiated with a homogeneous disorder: 72 Mg and 144 Nb sites are randomly assigned to the lattice. We use the order parameter $O(s) = \frac{1}{6N_B} \sum_{i \sim j} s_i s_j$ to monitor the formation of a Nb-rich sublattice. $N_B = 216$ is the total number of B sites. i is summed over the indices of all B sites. j is summed over the six nearest neighbor B sites of site- i . We let $s_i = +1$ for the Nb site and $s_i = -1$ for the Mg site. A homogeneous disorder leads to a positive O . If an all-Nb sublattice forms, O is $-\frac{1}{3}$. Indeed, the simulation shows that (Fig. 2(a)) $O(s)$ drops to $-\frac{1}{3}$ within 10^4 iterations of the FIRE-Swap simulation, where 303 swaps are accepted. ΔE_n of accepted swaps sum into roughly 75meV/f.u.

The optimized CS shows an artifact due to finite size effects: the Nb in β^{I} forms a cluster, leading to roughly a $(\text{PbNbO}_3)_2(\text{PbNb}_{1/2}\text{Mg}_{1/2}\text{O}_3)_4$ superlattice structure [44]. This artifact implies a certain phase separation of the Nb clusters and the rock-salt clusters—they can mix without changing the composition of sublattice β^{II} . But the supercell here ($N_B = 216$) is too small to relax the interface between clusters.

We remove the artifact and unfold the mesoscale structure by performing a FIRE-Swap simulation of a $12 \times 12 \times 12$ ($N_B = 1728$) supercell, which allows the interface to freely relax with $T_{\text{FS}} = 600\text{K}$. To accelerate optimization, the initial CS is generated according to the random-site model. Here, a formal definition of Nb cluster is in order. A Nb site belongs to a Nb cluster if it has at most one Mg-site neighbor among its six nearest neighbors. All such Nb sites form a subgraph of the lattice. The subgraph can be uniquely partitioned into its connected components, i.e. clusters. Different clusters are disconnected on the lattice. The size of a Nb cluster is the number of Nb sites it contains. For any given CS, the Breadth-First Search algorithm [45, 46] allows us to compute the size distribution of Nb clusters and identify the largest cluster. The initial CS of the supercell

has around 300 Nb sites that belong to about 250 Nb clusters. The largest cluster has a size of 17.

Fig. 2(b) shows results of the simulation, where around 4000 swaps are accepted from 3×10^5 iterations. ΔE_n of accepted swaps sum into roughly 20meV/f.u. Through the simulation, $O(s)$ stays within $[-1/3, -0.3]$. The number of Nb sites in Nb clusters increases to around 430 (gray curve), which has to be smaller than $N_B/3$, an upper bound [47] corresponding to a maximal separation of Nb clusters and rock-salt clusters. A major finding here is that the size of the largest Nb cluster increases from 17 to around 400 (blue curve). Almost all Nb sites in clusters collapse into the largest cluster that percolates the lattice, leaving only a few other clusters of merely size 1. Those Nb sites not in Nb clusters are mostly embedded in the rock-salt cluster [48] and belongs to sublattice β^{II} . We identified two anomalies beyond the typical phenomenology of phase separation. First, the surface of the largest Nb cluster does not coarsen to minimize interfacial energy (see Fig. 3(b) for an additional illustration). The surface to volume ratio η of the largest Nb cluster is larger than 2 throughout the simulation. For comparison, a perfect cubic cluster with volume $N_B/3$ gives $\eta < 1$. Second, the percolation theory on sublattice β^{I} prescribes a power-law distribution of the cluster size, suggesting substantially more clusters of intermediate size. The first anomaly is an electrostatic effect. The energy of an evenly charged spherical domain scales faster than the volume law, which forbids coarsening and leads the Nb cluster to take a mesh-like geometry. The second anomaly is expected, since the Nb ions anchored in sublattice β^{II} significantly facilitate the formation of a dominant Nb cluster and make the standard theory of percolation irrelevant.

We have revealed the major compositional features of the anchored-mesh model. How does it further describe the geometric and dipolar properties of PMN? We perform NVT MD simulations of the $12 \times 12 \times 12$ su-

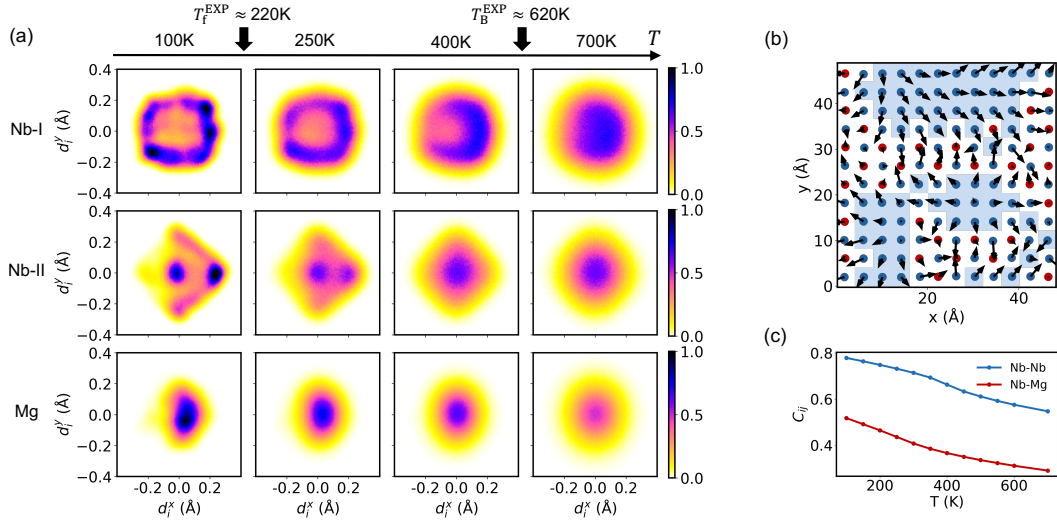


FIG. 3. (a) Histograms of PDF $p(d_i^x, d_i^y)$ associated with different types of B sites and different temperatures. The PDF $p(d_i^x, d_i^z)$ has similar features and are omitted here. (b) (d_i^x, d_i^y) as arrows on an arbitrary perovskite layer (in the XY plane) of the simulation box. Blue shades mark the Nb sites (blue spheres) in Nb clusters. Red sphere represents a Mg site. (c) The correlation functions C_{ij} (averaged over eligible pairs) for nearest-neighbor Nb-Nb pairs and Nb-Mg pairs .

percell with the optimized CS, for a thermal temperature T between 100K and 700K, each lasting 10ns. For $T = 300\text{K}$, we calculate the spherically symmetrized structure factor $S(Q)$ with standard Neutron scattering lengths [49]. The pair distribution function $H(r) \propto r^{-1} \int_0^\infty Q(S(Q) - 1) \sin(Qr) dQ$ is plotted in Fig. 2(c) for direct comparison with the measurements in PMN powder samples [50]. The general agreement is impressive. A minor but notable discrepancy is found near $r \approx 2.5\text{\AA}$, where predicted $H(r)$ exhibits a small peak that is invisible in experiments. The atomic origin of the peaks in $H(r)$ is illustrated by the lower panel of Fig. 2(c), which reports relevant radial distribution functions consistently predicted for $T = 300\text{K}$. We find that the small peak near $r \approx 2.5\text{\AA}$ in predicted $H(r)$ is associated with Pb-O pairs, which exhibit a wide distribution within $[2.25, 3.5]\text{\AA}$, in close agreement with the wide Pb-O peaks (one at $r \approx 2.4\text{\AA}$ and strengthened below room temperature) in the same interval found by the X-ray scattering of the same sample [51]. So, the discrepancy appears to be a minor issue.

To study dipolar properties, we focus on the displacement \mathbf{d}_i of any B-site ion- i away from the geometric center of its oxygen octahedron cage. \mathbf{d}_i is strongly correlated with local (primitive-cell) dipole moments [52], and the softening of its vibration is a signature of ferroelectric phase transition [9]. The displacement of the A-site ion (Pb) from neighboring oxygen ions can also describe local polarity [26, 29], but it is less informative here regarding the interplay of CS and local polarity. At low temperature, the behaviors of \mathbf{d}_i for B sites in different clusters are found to be drastically different. The sharp contrast is shown by Fig. 3(a), which depicts the proba-

bility density function (PDF) $p(d_i^x, d_i^y)$ of Nb ions in the Nb cluster (Nb-I for brevity), Nb ions in the rock-salt cluster (Nb-II), and generic magnesium ions.

In general, the features of the PDFs are consistent with the phenomenology of different stages of relaxor ferroelectricity. Above the so called Burns temperature $T_B \approx 620\text{K}$ [2], the PDF associated with Nb-I, Nb-II, and Mg all display spherical symmetry, signifying a trivial paraelectric state. Below T_B and above the freezing temperature $T_f \approx 220\text{K}$ [5], there are signs of quenching disorder in \mathbf{d}_i of Nb-I and Nb-II. Below T_f , the disorder in \mathbf{d}_i of Nb-I and Nb-II is substantially quenched, in other words frozen, which is associated with the so called non-ergodic relaxor phase. Meanwhile, the variation in the PDFs associated with Mg ions is much less drastic. Hence, the polar fluctuation associated with Mg ions plays a minor role in shaping dielectric properties.

Many qualitative differences between Nb-I and Nb-II can be identified from the PDFs. Some are finite size effects due to insufficient self-averaging, such as the weak breaking of mirror symmetry (e.g. $x \rightarrow -x$) in the PDF, which is evident for $T \leq 250\text{K}$. One may eliminate this artifact by simulating a larger supercell optimized by FIRE-Swap. Here, we examine the essential difference that is not obscured by finite size effects and, meanwhile, is most relevant to how CS shapes relaxor ferroelectricity: the PDF of Nb-I at $T = 100\text{K}$ displays a continuous distribution of disorder, while the PDF of Nb-II is much less diffusive and has strong separated peaks. It is implied that Nb-II should be less electrically susceptible than Nb-I because of its rigidity. The flexible \mathbf{d}_i of Nb-I and its continuous distribution are reminiscent of polar nanoregions (PNRs) [20, 53–57] postulated as the

key mechanism of relaxor ferroelectricity.

To illustrate PNRs, we show in Fig. 3 a snapshot of (d_i^x, d_i^y) on one layer (in the XY plane) of the supercell. Indeed, neighboring \mathbf{d}_i in the Nb cluster appear to be strongly correlated but flexible, potentially subject to reorientation under external fields. In the anchored-mesh model, the PNRs of these correlated Nb sites are not separated on a disordered matrix to interact like discrete and frustrated “mesoscopic dipoles”. The phenomenological picture of individual spherical nanosized PNRs [20, 58] seems to be imprecise. The equilibrium correlation function for neighboring \mathbf{d}_i and \mathbf{d}_j ($C_{ij} = \langle \mathbf{d}_i \mathbf{d}_j \rangle / \sqrt{\langle \|\mathbf{d}_i\|^2 \rangle \langle \|\mathbf{d}_j\|^2 \rangle}$) is shown in Fig. 3(c). C_{ij} for Nb pairs rises to almost 0.8 at $T = 100\text{K}$. This amounts to a substantial correlation length around 2nm. Meanwhile, C_{ij} for Nb-Mg pairs that reside in rock-salt clusters has a correlation length small enough that different Nb-II sites are almost uncorrelated.

Presumably, dielectric responses of PMN are shaped by the fluctuation in the percolating Nb cluster. We can not yet judge whether the unique properties (e.g., Vogel-Fulcher law [4]) of PMN should be attributed to the often postulated collective dipolar reorientation of PNRs. In principle, one can calculate the frequency-dependent dielectric permittivity $\epsilon(T)$ with our optimized CS. However, advanced enhanced sampling methods may be necessary to fill the huge gap between the typical time scale (ps~ns) in numerical simulation and that (ns~s) accessible to experiments. We leave this for future work.

In closing, our approach to construct the PES model and to perform FIRE-Swap and MD simulations can be applied to other relaxor ferroelectrics, opening a systematic route to modeling CS of generic perovskite solid solutions without uncontrolled assumptions.

Data and Code Availability – Data sets, models, and scripts that can reproduce the findings of this study will be publicly available on GitHub [59].

Acknowledgement – We thank Roberto Car and Peichen Zhong for fruitful discussions. VASP calculations were done when P.X. and K.C. were graduate students in Roberto Car’s group at Princeton, where the VASP license is issued. P.X. and K.C. developed the PES model with support from the Computational Chemical Sciences Center: Chemistry in Solution and at Interfaces (CSI), funded by the US Department of Energy (DOE) Award DE-SC0019394. Calculations were performed using the Princeton Research Computing resources at Princeton University, which is a consortium of groups led by the Princeton Institute for Computational Science and Engineering (PICSciE) and Office of Information Technology’s Research Computing. P.X. was then supported by the Alvarez Fellowship of Lawrence Berkeley National Lab. X.X. was supported by the Berkeley Lab 2025 Summer Program, where the majority of this work was performed. X.X. and P.X. were supported by the DOE Advanced Scientific Computing Research (ASCR) Applied

Mathematics program under Contract No. DE-AC02-05CH11231. This research mainly used resources of the National Energy Research Scientific Computing Center (NERSC), a Department of Energy User Facility, using AI4Sci@NERSC award DDR-ERCAP 34636.

* X.X. and K.C. contribute equally to this work

† pinchenxie@lbl.gov

- [1] G. A. Smolenskii, V. A. Isupov, A. I. Agranovskaya, and S. N. Popov, Ferroelectrics with diffuse phase transitions, Sov. Phys. – Solid State **2**, 2584 (1961).
- [2] G. Burns and F. H. Dacol, Glassy polarization behavior in ferroelectric compounds $\text{Pb}(\text{Mg}_{1/3}\text{Nb}_{2/3})\text{O}_3$ and $\text{Pb}(\text{Zn}_{1/3}\text{Nb}_{2/3})\text{O}_3$, Solid State Commun. **48**, 853 (1983).
- [3] G. Burns and F. H. Dacol, Crystalline ferroelectrics with glassy polarization behavior, Phys. Rev. B **28**, 2527 (1983).
- [4] D. Viehland, S. Jang, L. E. Cross, and M. Wuttig, Freezing of the polarization fluctuations in lead magnesium niobate relaxors, J. Appl. Phys. **68**, 2916 (1990).
- [5] D. Viehland, M. Wuttig, and L. Cross, The glassy behavior of relaxor ferroelectrics, Ferroelectrics **120**, 71 (1991).
- [6] A. Levstik, Z. Kutnjak, C. Filipič, and R. Raša, Glassy freezing in relaxor ferroelectric lead magnesium niobate, Phys. Rev. B **57**, 11204 (1998).
- [7] R. A. Cowley, S. N. Gvasaliya, S. G. Lushnikov, B. Roessli, and G. M. Rotaru, Relaxing with relaxors: a review of relaxor ferroelectrics, Adv. Phys. **60**, 229 (2011).
- [8] A. A. Bokov and Z.-G. Ye, Recent progress in relaxor ferroelectrics with perovskite structure, Prog. Adv. Dielectr. **1**, 105 (2020).
- [9] K. M. Rabe, C. H. Ahn, and J.-M. Triscone, *Physics of ferroelectrics: a modern perspective*, Topics in Applied Physics, Vol. 105 (Springer, Berlin, 2007).
- [10] D. Sherrington, Bzt: a soft pseudospin glass, Phys. Rev. Lett. **111**, 227601 (2013).
- [11] G. V. Lecomte, H. v. Löhneysen, and E. F. Wassermann, Frequency dependent magnetic susceptibility and spin glass freezing in ptmn alloys, Z. Phys. B **50**, 239 (1983).
- [12] J. Chen, H. M. Chan, and M. P. Harmer, Glassy polarization behavior in ferroelectric compounds $\text{Pb}(\text{Mg}_{1/3}\text{Nb}_{2/3})\text{O}_3$ and $\text{Pb}(\text{Zn}_{1/3}\text{Nb}_{2/3})\text{O}_3$, J. Am. Ceram. Soc. **72**, 593 (1989).
- [13] C. A. Randall, A. S. Bhalla, T. R. Shrout, and L. E. Cross, Classification and consequences of complex lead perovskite ferroelectrics with regard to B-site cation order, J. Mater. Res. **5**, 829 (1990).
- [14] C. Boulesteix, F. Varnier, A. Llebaria, and E. Husson, Numerical determination of the local ordering of $\text{Pb}(\text{Mg})_{1/3}\text{Nb}_{2/3}\text{O}_3$ (PMN) from high-resolution electron microscopy images, J. Solid State Chem. **108**, 141 (1994).
- [15] Z. Kutnjak, C. Filipič, R. Pirc, A. Levstik, R. Farhi, and M. El Marssi, Slow dynamics and ergodicity breaking in a lanthanum-modified lead zirconate titanate relaxor system, Phys. Rev. B **59**, 294 (1999).
- [16] P. Davies and M. Akbas, Chemical order in PMN-related relaxors: structure, stability, modification, and impact on properties, J. Phys. Chem. Solids **61**, 159 (2000).
- [17] M. A. Akbas and P. K. Davies, Thermally in-

duced coarsening of the chemically ordered domains in $\text{Pb}(\text{Mg}_{1/3}\text{Nb}_{2/3})\text{O}_3$ (PMN)-based relaxor ferroelectrics, *J. Am. Ceram. Soc.* **83**, 119 (2000).

[18] Z. Xu, S. M. Gupta, D. Viehland, Y. Yan, and S. J. Pennycook, Direct imaging of atomic ordering in undoped and La-doped $\text{Pb}(\text{Mg}_{1/3}\text{Nb}_{2/3})\text{O}_3$, *J. Am. Ceram. Soc.* **83**, 181 (2000).

[19] L. Farber and P. K. Davies, Influence of cation order on the dielectric properties of $\text{Pb}(\text{Mg}_{1/3}\text{Nb}_{2/3})\text{O}_3$ – $\text{Pb}(\text{Sc}_{1/2}\text{Nb}_{1/2})\text{O}_3$ (PMN–PSN) relaxor ferroelectrics, *J. Am. Ceram. Soc.* **86**, 1861 (2003).

[20] D. Fu, H. Taniguchi, M. Itoh, S. y. Koshihara, N. Yamamoto, and S. Mori, Relaxor $\text{Pb}(\text{Mg}_{1/3}\text{Nb}_{2/3})\text{O}_3$: a ferroelectric with multiple inhomogeneities, *Phys. Rev. Lett.* **103**, 207601 (2009).

[21] M. J. Cabral, S. Zhang, E. C. Dickey, and J. M. LeBeau, Gradient chemical order in the relaxor $\text{Pb}(\text{Mg}_{1/3}\text{Nb}_{2/3})\text{O}_3$, *Appl. Phys. Lett.* **112** (2018).

[22] The formation of Nb-rich sublattice prevents the adjacency of Mg sites that presumably contribute a greater electrostatic repulsion than the adjacent Mg-Nb and Nb-Nb sites.

[23] M. Cantoni, S. Bharadwaja, S. Gentil, and N. Setter, Direct observation of the B-site cationic order in the ferroelectric relaxor $\text{Pb}(\text{Mg}_{1/3}\text{Ta}_{2/3})\text{O}_3$, *J. Appl. Phys.* **96**, 3870 (2004).

[24] C. D. Lorenz, R. May, and R. M. Ziff, Similarity of percolation thresholds on the HCP and FCC lattices, *J. Stat. Phys.* **98**, 961 (2000).

[25] S. Pennycook and L. Boatner, Chemically sensitive structure-imaging with a scanning transmission electron microscope, *Nature* **336**, 565 (1988).

[26] M. Eremenko, V. Krayzman, A. Bosak, H. Y. Playford, K. W. Chapman, J. C. Woicik, B. Ravel, and I. Levin, Local atomic order and hierarchical polar nanoregions in a classical relaxor ferroelectric, *Nat. Commun.* **10**, 2728 (2019).

[27] W. Zhong, D. Vanderbilt, and K. M. Rabe, First-principles theory of ferroelectric phase transitions for perovskites: The case of BaTiO_3 , *Phys. Rev. B* **52**, 6301 (1995).

[28] Y.-H. Shin, V. R. Cooper, I. Grinberg, and A. M. Rappe, Development of a bond-valence molecular-dynamics model for complex oxides, *Phys. Rev. B* **71**, 054104 (2005).

[29] H. Takenaka, I. Grinberg, S. Liu, and A. M. Rappe, Slush-like polar structures in single-crystal relaxors, *Nature* **546**, 391 (2017).

[30] A. R. Akbarzadeh, S. Prosandeev, E. J. Walter, A. Al-Barakaty, and L. Bellaiche, Finite-temperature properties of $\text{Ba}(\text{Zr,Ti})\text{O}_3$ relaxors from first principles, *Phys. Rev. Lett.* **108**, 257601 (2012).

[31] J. Zhang, L. Liu, A. A. Bokov, N. Zhang, D. Wang, Z.-G. Ye, and C.-L. Jia, Compositional ordering in relaxor ferroelectric $\text{Pb}(\text{BB}')\text{O}_3$: nearest-neighbor approach, *Phys. Rev. B* **103**, 054201 (2021).

[32] M. Widom, W. P. Huhn, S. Maiti, and W. Steurer, Hybrid monte carlo/molecular dynamics simulation of a refractory metal high entropy alloy, *Metall. Mater. Trans. A* **45**, 196 (2014).

[33] E. Antillon, C. Woodward, S. Rao, B. Akdim, and T. Parthasarathy, Chemical short range order strengthening in a model fcc high entropy alloy, *Acta Mater.* **190**, 29 (2020).

[34] J. Han, L. Zhang, R. Car, and W. E, Deep potential: A general representation of a many-body potential energy surface, *Commun. Comput. Phys.* **23**, 629 (2018).

[35] L. Zhang, J. Han, H. Wang, R. Car, and W. E, Deep potential molecular dynamics: a scalable model with the accuracy of quantum mechanics, *Phys. Rev. Lett.* **120**, 143001 (2018).

[36] L. Zhang, J. Han, H. Wang, W. A. Saidi, R. Car, *et al.*, End-to-end symmetry preserving inter-atomic potential energy model for finite and extended systems, in *Advances in Neural Information Processing Systems*, Vol. 31 (2018).

[37] J. Sun, A. Ruzsinszky, and J. P. Perdew, Strongly constrained and appropriately normed semilocal density functional, *Phys. Rev. Lett.* **115**, 036402 (2015).

[38] Y. Zhang, J. Sun, J. P. Perdew, and X. Wu, Comparative first-principles studies of prototypical ferroelectric materials by LDA, GGA, and SCAN meta-GGA, *Phys. Rev. B* **96**, 035143 (2017).

[39] P. Xie, Y. Chen, W. E, and R. Car, Thermal disorder and phonon softening in the ferroelectric phase transition of lead titanate, *Phys. Rev. B* **111**, 094113 (2025).

[40] B. Yang, P. Xie, and R. Car, Deuteration removes quantum dipolar defects from KDP crystals, *npj Comput. Mater.* **10**, 241 (2024).

[41] F. H. Stillinger and T. A. Weber, Inherent structure in water, *J. Phys. Chem.* **87**, 2833 (1983).

[42] D. Corti, P. Debenedetti, S. Sastry, and F. Stillinger, Constraints, metastability, and inherent structures in liquids, *Phys. Rev. E* **55**, 5522 (1997).

[43] N. Nakagawa and M. Peyrard, The inherent structure landscape of a protein, *Proc. Natl. Acad. Sci. U.S.A.* **103**, 5279 (2006).

[44] Repeating the optimization of the supercell with different random initial composition leads to almost identical results up to crystalline symmetry.

[45] E. F. Moore, The shortest path through a maze, in *Proc. of the International Symposium on the Theory of Switching* (Harvard University Press, 1959) pp. 285–292.

[46] C. Y. Lee, An algorithm for path connections and its applications, *IRE Trans. Electron. Comput.* **10**, 346 (1961).

[47] The upper bound cannot be reached because our definition of a Nb cluster omits those sites on interface.

[48] We verify this by tracking the number of Nb sites in the rock-salt cluster, and an Nb site belongs to a rock-salt cluster if it has at most one Nb neighbor. Details of the analysis are omitted but available in Supplementary Data and Code [59].

[49] Pb: 9.405fm, Mg: -3.73fm, Nb: 7.054fm, O: 5.803fm.

[50] See Supplementary Figure 1 of Ref. [26].

[51] See Supplementary Figure 17(a) of Ref. [26].

[52] The local dipole moment can be rigorously defined from the Wannier-center representation of the polarization prescribed by the berry-phase theory [60, 61] as in Ref. [39].

[53] S. Wakimoto, C. Stock, R. J. Birgeneau, Z.-G. Ye, W. Chen, W. J. L. Buyers, P. M. Gehring, and G. Shirane, Ferroelectric ordering in the relaxor $\text{Pb}(\text{Mg}_{1/3}\text{Nb}_{2/3})\text{O}_3$ as evidenced by low-temperature phonon anomalies, *Phys. Rev. B* **65**, 172105 (2002).

[54] R. Blinc, V. V. Laguta, and B. Zalar, Field-cooled and zero-field-cooled ^{207}Pb NMR and the local structure of relaxor $\text{Pb}(\text{Mg}_{1/3}\text{Nb}_{2/3})\text{O}_3$, *Phys. Rev. Lett.* **91**, 247601 (2003).

[55] I.-K. Jeong, T. Darling, J. Lee, T. Proffen, R. Heffner, J. Park, K. Hong, W. Dmowski, and T. Egami, Direct observation of the formation of polar nanoregions in $\text{Pb}(\text{Mg}_{1/3}\text{Nb}_{2/3})\text{O}_3$ using neutron pair distribution function analysis, *Phys. Rev. Lett.* **94**, 147602 (2005).

[56] P. M. Gehring, H. Hiraka, C. Stock, S.-H. Lee, W. Chen, Z.-G. Ye, S. B. Vakhrushev, and Z. Chowdhuri, Reassessment of the burns temperature and its relationship to the diffuse scattering, lattice dynamics, and thermal expansion in relaxor $\text{Pb}(\text{Mg}_{1/3}\text{Nb}_{2/3})\text{O}_3$, *Phys. Rev. B* **79**, 224109 (2009).

[57] A. Kumar, J. N. Baker, P. C. Bowes, M. J. Cabral, S. Zhang, E. C. Dickey, D. L. Irving, and J. M. LeBeau, Atomic-resolution electron microscopy of nanoscale local structure in lead-based relaxor ferroelectrics, *Nat. Mater.* **20**, 62 (2021).

[58] D. Fu, H. Taniguchi, M. Itoh, and S. Mori, $\text{Pb}(\text{Mg}_{1/3}\text{Nb}_{2/3})\text{O}_3$ (PMN) relaxor: dipole glass or nano-domain ferroelectric?, in *Advances in Ferroelectrics* (IntechOpen, London, 2012).

[59] Supplementary Data and Code, https://github.com/xuxinyu2820/PMN_COR, accessed: 2025-10-16.

[60] R. Resta and D. Vanderbilt, Theory of polarization: A modern approach, in *Physics of Ferroelectrics: A Modern Perspective* (Springer, Berlin, Heidelberg, 2007) pp. 31–68.

[61] N. Marzari, A. A. Mostofi, J. R. Yates, I. Souza, and D. Vanderbilt, Maximally localized wannier functions: Theory and applications, *Rev. Mod. Phys.* **84**, 1419 (2012).

[62] G. Kresse and J. Furthmüller, Efficient iterative schemes for ab initio total-energy calculations using a plane-wave basis set, *Phys. Rev. B* **54**, 11169 (1996).

[63] G. Kresse and J. Furthmüller, Efficiency of ab-initio total energy calculations for metals and semiconductors using a plane-wave basis set, *Comput. Mater. Sci.* **6**, 15 (1996).

[64] G. Kresse and D. Joubert, From ultrasoft pseudopotentials to the projector augmented-wave method, *Phys. Rev. B* **59**, 1758 (1999).

[65] H. Wang, L. Zhang, J. Han, and W. E, DeePMD-kit: A deep learning package for many-body potential energy representation and molecular dynamics, *Comput. Phys. Commun.* **228**, 178 (2018).

[66] D. Lu, H. Wang, M. Chen, L. Lin, R. Car, W. E, W. Jia, and L. Zhang, 86 PFLOPS deep potential molecular dynamics simulation of 100 million atoms with ab initio accuracy, *Comput. Phys. Commun.* **259**, 107624 (2021).

[67] J. Zeng, D. Zhang, D. Lu, P. Mo, L. Zhang, H. Wang, W. E, R. Car, *et al.*, DeePMD-kit v2: a software package for deep potential models, *J. Chem. Phys.* **159**, 054801 (2023).

[68] L. Zhang, D.-Y. Lin, H. Wang, R. Car, and W. E, Active learning of uniformly accurate interatomic potentials for materials simulation, *Phys. Rev. Mater.* **3**, 023804 (2019).

[69] Y. Zhang, H. Wang, W. Chen, J. Zeng, L. Zhang, H. Wang, and W. E, DP-GEN: a concurrent learning platform for the generation of reliable deep learning based potential energy models, *Comput. Phys. Commun.* **253**, 107206 (2020).

[70] L. Zhang, H. Wang, M. C. Muniz, A. Z. Panagiotopoulos, R. Car, and W. E, A deep potential model with long-range electrostatic interactions, *J. Chem. Phys.* **156**, 124107 (2022).

[71] D. S. King, D. Kim, P. Zhong, and B. Cheng, Machine learning of charges and long-range interactions from energies and forces, *Nat. Commun.* **16**, 8763 (2025).

[72] S. Falletta, A. Cepellotti, A. Johansson, C. W. Tan, M. L. Descoteaux, A. Musaelian, C. J. Owen, and B. Kozinsky, Unified differentiable learning of electric response, *Nat. Commun.* **16**, 4031 (2025).

APPENDIX

Appendix A - SCAN-based Deep Potential

We base our study of PMN on density functional theory with the SCAN approximation [37]. We use VASP [62, 63] and the projector augmented wave (PAW) potentials [64] for all DFT calculations. The semicore 2s-states are taken as valence states for O. The semicore 2p-states are taken as valence states for Mg. 5d, 6s, and 6p states are taken as valence states for Pb atoms. 4p, 5s, and 4d states are taken as valence states for Nb atoms. The energy cutoff of the plane-wave basis is set as 403.93 eV. The smallest allowed spacing between k-points is 0.6 \AA^{-1} . Gamma point is always included in the k-points.

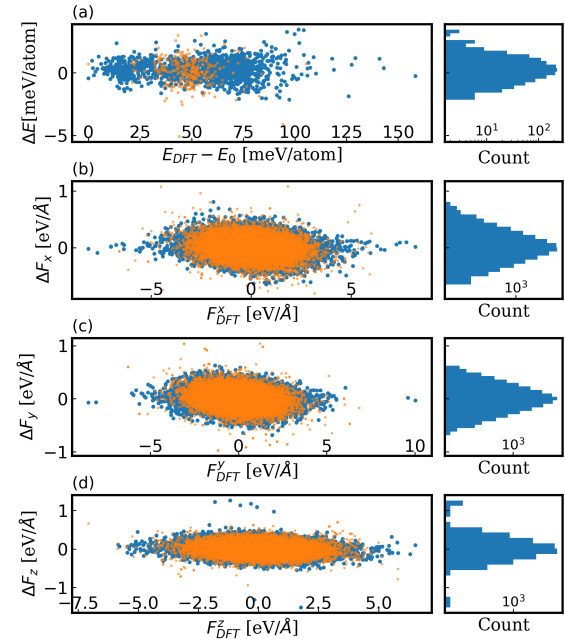


FIG. 4. Error distribution of the DP model. Blue trainset. orange test set

We train a Deep Potential model for PMN with DeePMD-Kit [65–67] based on SCAN-DFT. The atomic configurations in the data set are collected with the active learning framework DPGEN [68, 69] in the pressure interval $[1, 3 \times 10^4]$ bar and the temperature interval $[150, 650]$ K. The active exploration of configuration spaces is done with NPT-MD simulations starting from initial PMN configurations of different sizes and different disordering patterns. Specifically, there are three types

of initial configurations: (1) Charge-balanced supercells of 36 PMN units (180 atoms) prescribed by the random-site model; (2) Charge-balanced supercells of 72 PMN units prescribed by the random-site model; (3) Charge-balanced supercells of 27 PMN units where Nb and Mg ions are randomly distributed on the B-lattice in a 2:1 ratio.

The active learning procedure consists of 15 iterations of NPT-MD explorations. We used data from 12 iterations, together with the initial dataset manually generated before active learning, as the train set, which contains DFT energy and force labels for 1386 different atomic configurations. The data from the other 3 iterations are used as the test set, containing 300 different atomic configurations. With the train set, we obtain a DP model with a short-range cutoff 6 Å. Its error distribution in the train set and the test set is given by Fig. 4. We find a root-mean-squared error (RMSE) of 0.8 meV/atom and 1.0 meV/atom on the train set and the test set, respectively.

To further reduce error, one may consider long-range electrostatic interaction beyond the short-range cutoff, through computationally more intensive neural network potentials with an effective representation of electron charges [70–72]. We assume that such long-range correction should not affect the qualitative conclusions of our study. First, for non-equal-valence PMN, the formation of rock-salt ordering is partly the consequence of strong electrostatic repulsion between neighboring Mg-Mg sites (average ionic charge is -2e for a PbMgO_3 unit, +e for a PbNbO_3 unit). The disfavor of neighboring Mg-Mg sites stabilizes the Nb-rich sublattice β^{II} even in the absence of long-range electrostatic interaction beyond a reasonable short-range cutoff (at least 6 Å). Then, with the Nb-rich sublattice β^{II} established, it is natural that the excessive Nb sites on sublattice β^{I} going beyond the percolation threshold forms a mesh-like geometry to increase the surface to volume ratio η . A larger η means a larger interface between rock-salt clusters (negatively charged) and Nb clusters (positively charged), which stabilizes CS as a short-range interfacial effect and was preferred over spherical Nb clusters that constructively contribute to electrostatic repulsion. In the future, these conclusions can be further validated using larger-scale simulations and advanced models with long-range interaction. The FIRE-Swap algorithm itself does not need modification.

The initial configurations, the final datasets, and the scripts for DPGEN and DeePMD-kit are available at

[59].

Appendix B - Details of FIRE-Swap simulation

For all FIRE-Swap simulations reported in this paper, we use $T_{\text{FS}} = 600\text{K}$. And we use $0.02\text{eV}/\text{\AA}$ as the force threshold for a single FIRE simulation. The number of steps allowed for the FIRE simulation of the initial CS is unlimited. Otherwise, the maximum number of steps allowed for a single FIRE simulation is 200. The FIRE-Swap simulation is implemented with the FIRE module in the Atomic Simulation Environment (ASE) and the Python interface of the DeePMD-kit (code available at [59]).

Here we provide evidence for the claim in the main text that the contribution of atomic geometric disorder to system energy is comparable to that from compositional disorder. Relevant to this claim are two quantities: $\Delta E_{\text{FIRE}} = U(\mathbf{s}'_n, \mathbf{R}'_n) - U(\mathbf{s}'_n, \mathbf{R}^*_{n-1})$ and $\Delta E_{\text{Total}} = U(\mathbf{s}'_n, \mathbf{R}'_n) - U(\mathbf{s}^*_{n-1}, \mathbf{R}^*_{n-1})$, as indicated in the left panel of Fig. 5. The probability density distribution of ΔE_{FIRE} and ΔE_{Total} in the FIRE-Swap simulation of the $6 \times 6 \times 6$ supercell is plotted in the right panel of Fig. 5.

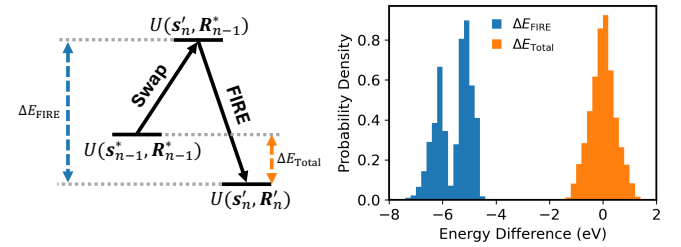


FIG. 5. Left panel: A sketch of energy changes, ΔE_{FIRE} and ΔE_{Total} , in one iteration of FIRE-Swap. Right panel: the probability density distribution of ΔE_{FIRE} and ΔE_{Total} in a FIRE-Swap simulation with around 10000 iterations.

The distribution of ΔE_{FIRE} is associated with the energy scale relevant to atomic geometric disorder. Let $\Delta E_{\text{Swap}} = \Delta E_{\text{Total}} - \Delta E_{\text{FIRE}}$. The distribution of ΔE_{Swap} is associated with the energy scale relevant to the compositional disorder. From Fig. 5, ΔE_{FIRE} is typically around -6 eV. Meanwhile, the distribution of ΔE_{Total} resembles a zero-centered Gaussian with a standard deviation smaller than 1 eV. This suggests that the distribution of ΔE_{Swap} will be centered around 6 eV. So, essentially, in a FIRE-Swap simulation, the energy changes caused by swapping B sites and by geometric optimization are of the same order. It is the small remnant of their cancellation determines the acceptance of a proposed new CS.